

A molecularly engineered hole-transporting material for efficient perovskite solar cells

Michael Saliba¹, Simonetta Orlandi², Taisuke Matsui³, Sadig Aghazada¹, Marco Cavazzini², Juan-Pablo Correa-Baena⁴, Peng Gao¹, Rosario Scopelliti¹, Edoardo Mosconi⁵, Klaus-Hermann Dahmen⁶, Filippo De Angelis⁵, Antonio Abate⁷, Anders Hagfeldt⁴, Gianluca Pozzi², Michael Graetzel⁷ and Mohammad Khaja Nazeeruddin^{1*}

Solution-processable perovskite solar cells have recently achieved certified power conversion efficiencies of over 20%, challenging the long-standing perception that high efficiencies must come at high costs. One major bottleneck for increasing the efficiency even further is the lack of suitable hole-transporting materials, which extract positive charges from the active light absorber and transmit them to the electrode. In this work, we present a molecularly engineered hole-transport material with a simple dissymmetric fluorene-dithiophene (FDT) core substituted by *N,N*-di-*p*-methoxyphenylamine donor groups, which can be easily modified, providing the blueprint for a family of potentially low-cost hole-transport materials. We use FDT on state-of-the-art devices and achieve power conversion efficiencies of 20.2% which compare favourably with control devices with 2,2',7,7'-tetrakis(*N,N*-di-*p*-methoxyphenylamine)-9,9'-spirobifluorene (spiro-OMeTAD). Thus, this new hole transporter has the potential to replace spiro-OMeTAD.

The perovskite materials, APbX₃ (A = methylammonium (MA), formamidinium (FA); X = Br, I), used for photovoltaics (PV) have remarkable properties, such as very large carrier diffusion length¹, high panchromatic absorption with a tunable band gap from 1.1 to 3.1 eV (ref. 2) and low non-radiative recombination rates³. These are the same physical properties that made perovskites attractive for various research fields ranging from lasing^{4,5}, light-emitting devices⁶ and photodetection^{7,8} to tandem applications^{9–11}. We attribute the step efficiency increases over the past years in large part to careful fine-tuning of the perovskite composition and the myriad of fabrication techniques^{12–17}. For example, Jeon and co-workers achieved one of the highest certified power conversion efficiencies (PCEs) of 17.9% by optimizing the anti-solvent method with a mixed perovskite precursor¹² that is similar to the technique used for this work (where we reach up to 20% PCE). With the increased quality of perovskite films, other avenues of improving the overall solar cell performance are under intense scrutiny. Specifically, there is a renewed interest in identifying hole-transporter materials (HTMs), other than polytriarylamine polymer (PTAA) and spiro-OMeTAD that can yield PCEs close to or even exceeding 20% (refs 18,19). This is due to polymeric HTMs having potential drawbacks for commercialization because of the inherent mass distribution (polydispersity), which leads to a more difficult characterization, batch-to-batch variation and lower purity. Small molecules on the other hand, have a distinct molecular structure with a precise molecular weight and are especially attractive for industrial production if they exhibit a

facile synthesis process with high purity and yield. Unfortunately spiro-OMeTAD, pioneered by our group for solid-state dye sensitized solar cells in 1998 (ref. 20), has a lengthy, expensive synthesis and requires costly sublimation steps for purification²¹. After nearly two decades, spiro-OMeTAD is still used in many labs worldwide, including our own. Despite tremendous efforts to replace spiro-OMeTAD, most suggested molecules^{22–33} have not yet reached PCEs of 20%, which require short-circuit current densities (J_{sc}) near the maximum of $\sim 25 \text{ mA cm}^{-2}$ (for band gaps of 1.55 eV as calculated for a full device stack by Ball *et al.*³⁴) while maintaining high fill factors (FFs) and open-circuit voltages (V_{oc}).

In this work, we introduce 2,7'-bis(bis(4-methoxyphenyl)amino)spiro[cyclopenta[2,1-b:3,4-b']dithiophene-4,9'-fluorene] (see Fig. 1a), hereafter FDT, as a new HTM originally designed to take advantage of the peculiar optoelectronic properties of spirocyclopentadithiophene derivatives³⁵.

Perovskite solar cells using FDT as a HTM compare favourably with spiro-OMeTAD, with efficiencies exceeding 20%. Simulations and crystallographic analysis indicate that the additional thiophene-iodine interaction may improve hole transfer at the FDT/perovskite interface. FDT can be dissolved in the more environmentally friendly toluene instead of chlorobenzene (CB). The lab synthesis costs of FDT are estimated at $\sim 60 \text{ US\$ g}^{-1}$, which is about a fifth of the costs of purified spiro-OMeTAD, and significant price drops are expected once the economies of scales apply, making FDT an attractive low-cost alternative to spiro-OMeTAD.

¹Group for Molecular Engineering of Functional Materials, Institute of Chemical Sciences and Engineering, École Polytechnique Fédérale de Lausanne, EPFL VALAIS, Rue de l'industrie 17, CP 440, CH-1951 Sion, Switzerland. ²Istituto di Scienze e Tecnologie Molecolari del Consiglio Nazionale delle Ricerche, CNR-ISTM, via Golgi 19, I-20133 Milano, Italy. ³Advanced Research Division, Materials Research Laboratory, Panasonic Corporation, 1006 Kadoma, Kadoma City, Osaka 571-8501, Japan. ⁴Laboratory for Photomolecular Science, Institute of Chemical Sciences and Engineering, École Polytechnique Fédérale de Lausanne, CH-1015-Lausanne, Switzerland. ⁵Computational Laboratory for Hybrid Organic Photovoltaics (CLHYO), CNR-ISTM, via Elce di Sotto 8, I-06123 Perugia, Italy. ⁶Qatar Environment and Energy Research Institute, Hamad Bin Khalifa University, PO Box 5825, Qatar. ⁷Laboratory of Photonics and Interfaces, Institute of Chemical Sciences and Engineering, École Polytechnique Fédérale de Lausanne, Lausanne CH-1015, Switzerland. *e-mail: mdkhaja.nazeeruddin@epfl.ch

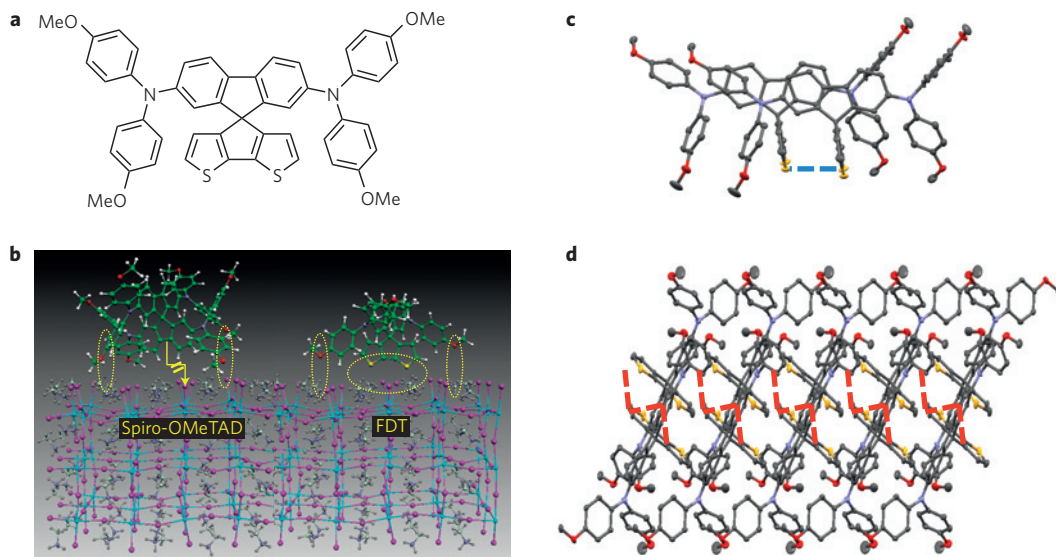


Figure 1 | XRD and simulation data of FDT. **a**, Molecular structure of 2',7'-bis(bis(4-methoxyphenyl)amino)spiro[cyclopenta[2,1-b:3,4-b']dithiophene-4,9'-fluorene], referred to as **FDT**. **b**, Docking of the spiro-OMeTAD and **FDT** on the MAI-terminated (110) perovskite surface. Highlighted are the attractive interactions between the HTMs and the perovskite. Note the lack of interaction between the spiro-OMeTAD core and the perovskite, which is switched on in the **FDT** HTM by the dithiophene core. **c**, Drawings and perspective views of two **FDT** molecules determined by X-ray crystallography with 50% probability thermal ellipsoids. Blue dashed line indicates the distance between the ring centroids (4 Å face to face). (Hydrogen atoms omitted for clarity). **d**, View down the reciprocal cell axis c^* of the stacking molecules. Dashed red lines illustrate $S \cdots S$ short contacts (3.33 and 3.46 Å).

Synthesis and characterization

FDT was conveniently prepared in over 80% yield by palladium catalysed cross-coupling of bis(4-methoxyphenyl)amine with a preformed dibromo spiro compound. The latter was obtained by mild intramolecular cyclization of a tertiary alcohol derived from 2,7-dibromofluorenone and protected 2,2'-dithiophene (see the synthesis scheme in Supplementary Note 1 for more details). **FDT** can be purified by standard column chromatography instead of costly sublimation procedures as in the case of spiro-OMeTAD. This is relevant for industrial applications where large-scale chromatographic separation techniques, such as simulated or counter-current moving bed chromatography, are used.

The structure of **FDT** is fully characterized by nuclear magnetic resonance (NMR) (^1H , ^{13}C , ^1H - ^{13}C heteronuclear single quantum coherence; Supplementary Figs 1–5) and mass spectrometry (electrospray ionization quadrupole time-of-flight; Supplementary Figs 6 and 7).

Thermogravimetric analysis indicates that **FDT** starts decomposing at 400 °C and spiro-OMeTAD at 445 °C (Supplementary Fig. 8a), which are both far above temperatures for conventional device operation. From differential scanning calorimetry measurements (Supplementary Fig. 8b), we find a melting temperature of 200 °C and a glass transition temperature of 110 °C for **FDT**. These temperatures are slightly below those for spiro-OMeTAD, which has a melting temperature of 245 °C and a glass transition temperature of 120 °C, agreeing well with Malinauskas and co-workers³⁶.

Crystallography and simulations

We use X-ray crystallography to analyse single crystals grown from an **FDT** solution left to dry. In the crystal lattice, **FDT** molecules stack in a slipped fashion via the cyclopentadithiophene (CPDT) planes along the b -axis (Fig. 1c) through CH/π hydrogen bonds and π - π interactions. Remarkably, extremely short intermolecular $S \cdots S$ contacts (3.33 and 3.46 Å) were found between the neighbouring columns related by an inversion centre (see Fig. 1d). We suggest that this dual-channel fashion interacts with the perovskite, facilitating a highly efficient

hole-transport system, and show further crystallographic analysis in Supplementary Note 2 (including Supplementary Figs 9–11 and Supplementary Table 1).

First-principles simulations carried out on the spiro-OMeTAD interface with MAPbI_3 (refs 37,38) revealed that the HTM/perovskite interaction occurred mainly between the HTM methoxy groups and the perovskite methylammonium sites, whereas the interaction with the surface iodine atoms was repulsive³⁷. Docking of the spiro-OMeTAD and of the **FDT** HTMs on the perovskite surface (Fig. 1b) reveals an additional interaction between the dithiophene **FDT** core and the perovskite surface, possibly mediated by the thiophene-iodine interaction³⁹. This may suggest a stronger adhesion and enhanced interfacial coupling between **FDT** and perovskite. The photogenerated hole delocalized on the perovskite iodine atoms, mainly contributing to the perovskite valence band⁴⁰, can thus be effectively transferred to the HTM, exploiting the additional thiophene-iodine interaction characterizing the **FDT**/perovskite interface. This may also provide an alternative hole-transfer pathway compared to spiro-OMeTAD.

In Fig. 2a, we investigate the absorption of spin-coated films of **FDT** and spiro-OMeTAD dissolved in CB and with the commonly used Li-TFSI, tBP and Co-complex⁴¹. The spectra are similar, showing that both **FDT** and spiro-OMeTAD are partially oxidized (owing to the Co-complex) and absorb in the visible region, as reported by Bach and co-workers²⁰. The absorption at ~ 430 nm (or 2.88 eV) coincides with the pristine, unoxidized material (not shown)¹⁶. In the inset of Fig. 2a, we complement this data with differential pulse voltammetry measurements of the pristine material. **FDT** exhibits two reversible couples, centred at 0.72 and 0.86 V versus the normal hydrogen electrode (NHE), showing excellent electrochemical stability, as compared to spiro-OMeTAD with three couples, centred at 0.70, 0.83 and 1.03 V versus the NHE, showing that the highest occupied molecular orbital (HOMO) levels are centred on the bis(4-methoxyphenyl)amino group. From this, we can derive the HOMO level of **FDT** at 5.16 eV and for spiro-OMeTAD at 5.14 eV, respectively. Thus, with the above absorption onset at 2.88 eV, the lowest unoccupied molecular orbital (LUMO) level of **FDT** is at 2.28 eV and for spiro-OMeTAD

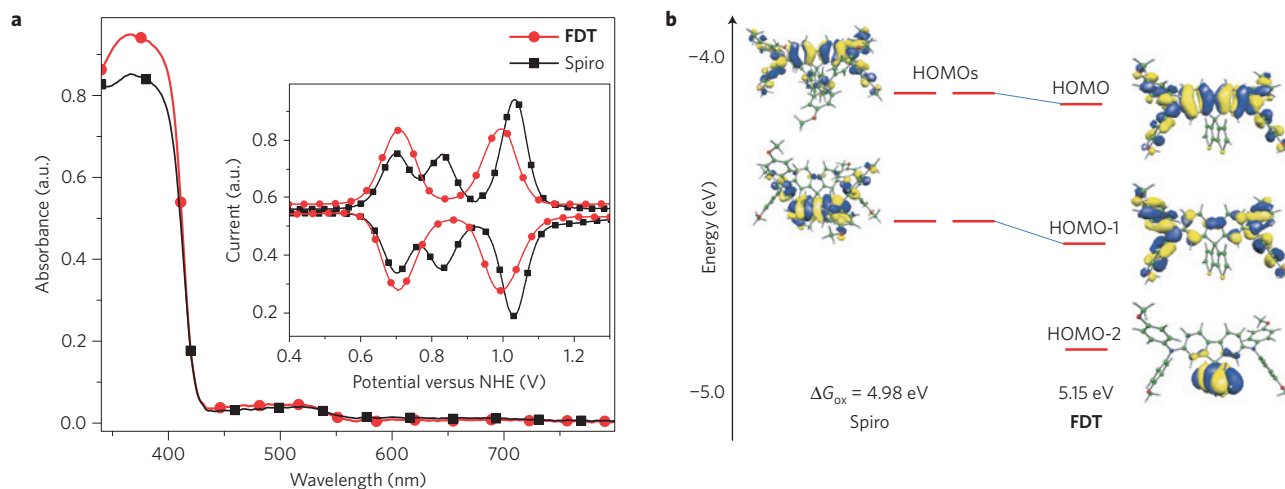


Figure 2 | Optical characterization and energy levels of FDT and spiro. **a**, Ultraviolet-visible absorption spectra of the **FDT** (circles) and spiro-OMeTAD (squares) from spin-coated films on microscope slides, prepared from chlorobenzene and with the commonly used Li-TFSI, tBP and Co-complex. Inset: differential pulse voltammetry measured in 0.1 M dichloromethane solution of NBu_4PF_6 . A glassy-carbon working electrode, and platinum wire counter and reference electrodes were used with ferrocene as an internal standard. The ferrocene oxidation potential was positioned at 0.7 V versus the normal hydrogen electrode (NHE) and the oxidation potentials of HTMs were recalculated and presented for ferrocene-free solutions. **b**, DFT-calculated electronic structure of the spiro-OMeTAD and **FDT**, showing electronic energy levels, HOMO plots and calculated adiabatic oxidation potentials. ΔG_{ox} is the Gibbs free energy of oxidation.

at 2.26 eV. The electronic structures of the spiro-OMeTAD and **FDT** HTMs calculated by density functional theory (DFT) are rather similar (see Fig. 2b), except that in spiro-OMeTAD the orbitals are almost doubly degenerate owing to the presence of two symmetric molecular halves. The HOMO of **FDT** (HOMO and HOMO-1 in spiro-OMeTAD) are delocalized on the methoxy-substituted phenylamine and spiro moieties, whereas the HOMO-1, lying at ~ 0.5 eV below the HOMO (HOMO-2 and HOMO-3 in spiro-OMeTAD) is mainly localized on the methoxy-substituted phenylamine moieties. The HOMO-2 of **FDT**, lying ~ 0.4 eV below the HOMO-1, is localized on the CPDT ligand, which is not paralleled in spiro-OMeTAD. The **FDT** HOMO is stabilized slightly relative to spiro-OMeTAD, as reflected in the higher calculated adiabatic oxidation potential for **FDT** compared to spiro-OMeTAD (5.15 versus 4.98 eV, see Fig. 2b), in good agreement with the experimental CV data. The slight HOMO stabilization in **FDT**, reflected in the higher oxidation potential, is due to the lack of repulsive interactions between the two molecular halves in spiro-OMeTAD, which raises the HOMO in the latter.

Device characterization

We use both **FDT** and spiro-OMeTAD to fabricate devices and show in Fig. 3a, a cross-sectional scanning electron microscopy (SEM) image of a full device stack with mixed perovskite (containing mixed MA and FA cations, with I and Br anions). The optimized thickness of the **FDT** layer is about ~ 170 nm, which is slightly below the optimized thickness for spiro-OMeTAD of ~ 200 nm.

In Fig. 3b, we present the current density–voltage (JV) scans for our champion devices for mixed perovskite with either **FDT** or spiro-OMeTAD as the HTM, respectively, with all extracted JV parameters in the inset table (as well as in Supplementary Table 2). We outline the fabrication details in the Supplementary Information. Our measurements were taken at a slow scan rate of 10 mV s^{-1} , resembling quasi steady-state conditions, as suggested independently by Unger *et al.* and Kamat and co-workers^{42,43}. The full hysteresis loop—that is, forward and backward scans—with the corresponding performance parameter for each device are reported in Supplementary Table 3.

For the mixed perovskite, the **FDT** hole transporter reaches 20.2%, on par with the highest reported PCEs so far, with a

short-circuit current (J_{sc}) of 22.7 mA cm^{-2} , an open-circuit voltage (V_{oc}) of 1,148 mV, and a FF of 0.76, narrowly outcompeting the best spiro-OMeTAD control with a PCE of 19.7%. We show the external quantum efficiency for a representative **FDT** device in Fig. 3c and achieve integrated current densities of 21.3 mA cm^{-2} , which are in close agreement with the JV scans. Moreover, we have investigated pure MAPbI_3 and MAPbBr_3 (shown in Supplementary Fig. 12 and Supplementary Table 2) perovskites with **FDT**, which exhibit efficiencies of 18.4% and 5.6%, respectively. Under comparable conditions the spiro-OMeTAD based controls yield 17.9% and 4.4%, respectively.

Our spiro-OMeTAD controls perform exceptionally well. Certainly, the values for the mixed and pure triiodide perovskite are among the highest reported (respectively, 17.9% by Jeon *et al.*¹² and 19.7% by Ahn *et al.*¹⁹), with open-circuit voltages comfortably exceeding 1.1V and no loss in FF. Even the performance values obtained for MAPbBr_3 are acceptable, with high voltages, albeit falling short of the values reported by Sheng and co-workers⁴⁴, who used an optimized vapour-assisted deposition method.

Overall, the perovskite layer must be of very high quality to achieve such peak performances, forming almost perfect contacts with the electron and hole selective layers, as can be seen in Fig. 3a. By exceeding most literature values, our state-of-the-art controls are the appropriate litmus tests to assess if **FDT** indeed has the potential to replace spiro-OMeTAD as a workhorse material.

We have been able to repeat these results on a regular basis for many batches over many months. To illustrate this, we show device statistics in Supplementary Fig. 10 for the mixed perovskite, comparing **FDT** and spiro-OMeTAD of at least 41 devices. We conducted a first stability assessment for unencapsulated **FDT** and spiro-OMeTAD devices stored under dry conditions in the dark. In Supplementary Fig. 14, we show that two months after preparation, there is almost no degradation during this time.

It is noteworthy that all **FDT** films are deposited from toluene solutions. **FDT** was more easily soluble than spiro-OMeTAD in both CB and toluene. For toluene, we could not get relevant concentrations of greater than 50 mM for spiro-OMeTAD. This matters, because halogenated solvents, such as CB, are an obstacle for industrial production owing to their toxicity and negative impact on the environment. Therefore, moving towards greener solvents

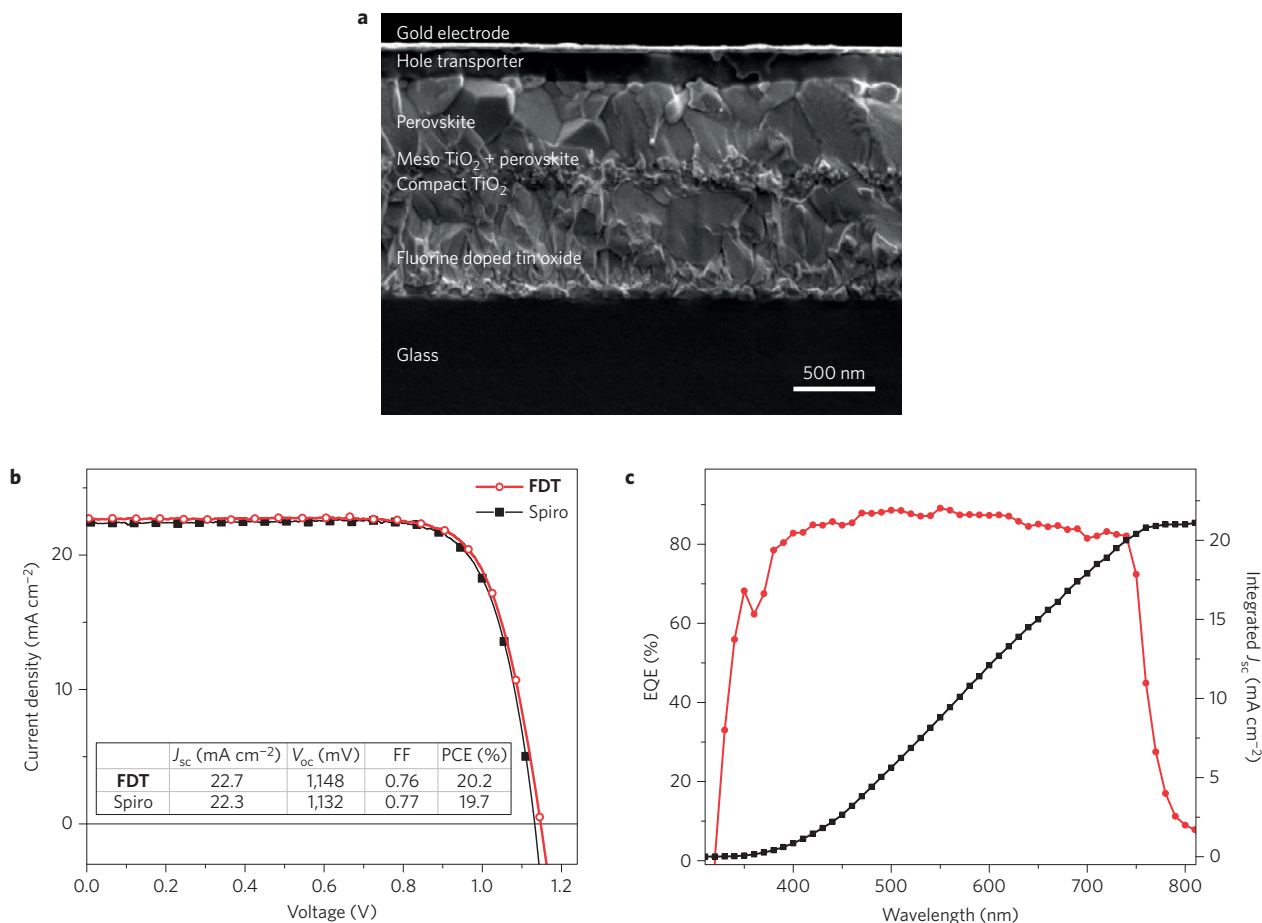


Figure 3 | Cross-sectional image of a full device together with the champion efficiencies of FDT and spiro. **a**, Cross-sectional SEM of a full device stack with mixed perovskite. **b**, Best performing JV scans collected under AM 1.5 simulated sunlight for **FDT** (open circles) and spiro-OMeTAD (solid squares) on mixed perovskite, alongside the extracted performance parameters in the table (inset). The voltage scan rate was 10 mV s^{-1} and no device preconditioning, such as prolonged light soaking or forward voltage bias, was applied before starting the measurement. The full hysteresis loop (forward and backward scan) for each scan is listed in Supplementary Table 3. **c**, External quantum efficiency (EQE; circles) of a representative **FDT** device with mixed perovskite. The integrated short-circuit current density (squares) of 21.3 mA cm^{-2} follows closely the JV scans from the solar simulator.

has been a major interest in the related field of organic PVs (ref. 45). Thus, replacing CB with toluene brings us one step closer to a more environmentally friendly HTM for perovskite solar cells.

With these results, we have found a new HTM that can match and exceed the performances of spiro-OMeTAD for the highest performance applications. This gives us more scope for understanding and improving perovskite solar cells.

Furthermore, the dissymmetrical fluorene–dithiophene core of **FDT** can be modified easily through well-established methods such as transition metal-catalysed cross-coupling reactions. We can, for example, fine-tune the HOMO levels to match the valence bands of an according perovskite or solid-state solar cell. Modifications are not restricted to the fluorene part; we can also alter the thiophene groups to add functionalities such as thermal stability, passivation of the underlayer, hydrophobic protection from moisture, and so on.

Conclusion

In summary, we have molecularly engineered the novel small molecule **FDT** HTM and compared perovskite-based solar cells prepared with **FDT** and with spiro-OMeTAD. The **FDT** devices compared favourably to spiro-OMeTAD in all performance tests, yielding PCEs up to 20.2%, which is one of the highest (uncertified) reported values for small molecule HTMs. Already, there is a distinct advantage in using **FDT** because it can be dissolved in the more environmentally friendly toluene instead of CB. Synthetically, the

FDT core can easily be modified and therefore might provide the blueprint for a family of high-performance HTMs. The lab synthesis costs of **FDT** are estimated following the procedure proposed by Osedach *et al.*⁴⁶ and recently applied by Petrus *et al.*²⁷, resulting in $\sim 60 \text{ US\$ g}^{-1}$ (see Supplementary Note 3 with Supplementary Tables 4–6 for a detailed calculation). This is about a fifth of the costs of purified spiro-OMeTAD ($\sim 500 \text{ US\$ g}^{-1}$, high purity, Merck) and we expect significant price drops once the economies of scale apply. Therefore, **FDT** has the potential to become a lower-cost alternative or possibly replace spiro-OMeTAD.

Methods

Substrate preparation and Li-doping TiO_2 . Nippon Sheet Glass 10Ω per square was cleaned by sonication in 2% Hellmanex water solution for 30 min. After rinsing with deionized water and ethanol, the substrates were further cleaned with ultraviolet ozone treatment for 15 min. Then, a 30 nm TiO_2 compact layer was deposited on FTO via spray pyrolysis at 450°C from a precursor solution of titanium diisopropoxide bis(acetylacetonate) in anhydrous ethanol. After the spraying, the substrates were left at 450°C for 45 min and then allowed to cool down to room temperature. Then, mesoporous TiO_2 layer was deposited by spin coating for 20 s at 4,000 r.p.m. with a ramp of $2,000 \text{ r.p.m. s}^{-1}$, using 30 nm particle paste (Dyesol 30 NR-D) diluted in ethanol to achieve a 150–200 nm layer thickness. After the spin coating, the substrates were immediately dried at 100°C for 10 min and then sintered again at 450°C for 30 min under dry air flow.

Li-doping of mesoporous TiO_2 is accomplished by spin coating a 0.1 M solution of Li-TFSI in acetonitrile at 3,000 r.p.m. for 30 s, followed by another sintering step at 450°C for 30 min. After cooling down to 150°C the substrates

were immediately transferred in a nitrogen atmosphere glove box to deposit the perovskite films.

Perovskite precursor solution and film preparation. The ‘mixed perovskite’ precursor solution contained FAI (1 M), PbI₂ (1.1 M), MABr (0.2 M) and PbBr₂ (0.2 M) dissolved in anhydrous DMF:DMSO 4:1 (v:v). The pure MAPbI₃ precursor was composed of PbI₂ (1.2 M) and MAI (1.2 M) dissolved in anhydrous DMSO. The pure MAPbBr₃ precursor was composed of PbBr₂ (1.2 M) and MABr (1.2 M) dissolved in anhydrous DMF:DMSO 4:1 (v:v).

The respective perovskite solution was spin-coated in a two-step procedure at 1,000 and 6,000 r.p.m. for 10 and 30 s respectively. During the second step, 100 μ l of chlorobenzene was poured on the spinning substrate 15 s before the end of the procedure. The substrates were then annealed at 100 °C for 1 h in a nitrogen atmosphere glove box.

Hole-transporting layer and top electrode. After the perovskite annealing, the substrates were cooled down for a few minutes and a spiro-OMeTAD (Merck) solution (70 mM in chlorobenzene) was spin-coated at 4,000 r.p.m. for 20 s. Spiro-OMeTAD was doped with bis(trifluoromethylsulphonyl)imide lithium salt (Li-TFSI, Sigma-Aldrich), tris(2-(1H-pyrazol-1-yl)-4-tert-butylpyridine)-cobalt(III) tris(bis(trifluoromethylsulphonyl)imide) (FK209, Dynamo) and 4-tert-butylpyridine (TBP, Sigma-Aldrich). The molar ratio of additives for spiro-OMeTAD was 0.5, 0.03 and 3.3 for Li-TFSI, FK209 and TBP, respectively.

FDT solutions were prepared with molarities ranging from 50 to 150 mM (in chlorobenzene or toluene). The optimized molar ratio of additives for **FDT** was 0.5, 0.03 and 3.3 for Li-TFSI, FK209 and TBP, respectively. The **FDT** solution was spin-coated at 4,000 r.p.m. for 20 s.

Finally, 70–80 nm of gold top electrode was thermally evaporated under high vacuum.

Photovoltaic device testing. The solar cells were measured using a 450 W xenon light source (Oriel). The spectral mismatch between AM1.5G and the simulated illumination was reduced by using a Schott K113 Tempax filter (Präzisions Glas & Optik GmbH). The light intensity was calibrated with a Si photodiode equipped with an infrared cutoff filter (KG3, Schott), and was recorded during each measurement. Current–voltage characteristics of the cells were obtained by applying an external voltage bias while measuring the current response with a digital sourcemeter (Keithley 2400). The voltage scan rate was 10 mV s⁻¹ and no device preconditioning, such as prolonged light soaking or forward voltage bias, was applied before starting the measurement. The starting voltage was determined as the potential at which the cells furnishes 1 mA in forward bias, no equilibration time was used. The cells were masked with a black metal mask (0.16 cm²) to fix the active area and reduce the influence of the scattered light.

Differential scanning calorimetry (DSC) was conducted on a DSC8000 calorimeter from PerkinElmer using 2–4 mg of sample powder placed in an aluminium pan with a tight-fitting lid. The scans were taken from –50 °C to 300 °C at a rate of 10 °C min⁻¹ in a nitrogen atmosphere.

Thermal gravimetric analysis (TGA) was performed on a TGA 4000 (PerkinElmer), heating steadily at constant rates of 10 °C min⁻¹ under a constant nitrogen gas flow of 20 ml min⁻¹. The investigated temperature intervals were between a minimum of 30 °C to a maximum of 900 °C. Ceramic crucibles and approximately 5–15 mg of sample material were used for each measurement.

Ultraviolet–visible measurements were performed on a Varian Cary 5. Scanning electron microscopy (SEM) was performed on a ZEISS Merlin HR-SEM.

Differential pulse voltammetry (DPV). Differential pulse voltammetry measurements were conducted with a Bio-Logic SP200 potentiostat in a deoxygenated 0.1 M dichloromethane solution of NBu₄PF₆ under nitrogen atmosphere. A glassy-carbon working electrode and platinum wire counter and reference electrodes were used. Measurements were carried out with ferrocene as an internal standard. The oxidation potential of ferrocene was positioned at 0.7 V versus the normal hydrogen electrode (NHE) potential, so the oxidation potentials of HTMs were determined versus the NHE.

Computational details The electronic properties and the geometry optimizations of the isolated spiro-OMeTAD and **FDT** are carried out with the Gaussian09 [Gaussian, Wallingford, Connecticut, 2009] program package using the B3LYP (ref. 47) exchange–correlation functional and the 6-31g* basis set⁴⁸.

Geometry optimizations of the interface models were carried out at the PBE-GGA (ref. 49) level with the SIESTA 3.0 program package⁵⁰ using a DZ basis set along with the PBE scalar-relativistic pseudopotential for I, S, O, C, N, and H atoms. Pb atoms were treated with the WC-GGA (ref. 51) scalar-relativistic pseudopotential. Electrons from I 5s, 5p; S 3s, 3p; O, N, and C 2s, 2p; H 1s; Pb 6s, 6p, 5d shells were explicitly included in the calculations. A value of 100 Ry was used as the plane wave cutoff for the grid. Spin–orbit interactions were not included in the SIESTA calculations.

By following the approach reported in our previous works^{52,53}, the model system was made of a 3 × 5 × 3 pseudocubic perovskite slab exposing the 110 surfaces. The perovskite slab stoichiometry was MA60Pb45I150 (thus, deviating from the ideal material stoichiometry) in line with the analysis of perovskite surfaces by Mitzi⁵⁴. To model the interface between perovskite and spiro-OMeTAD or **FDT**, we deposited the HTMs on one side of the perovskite slab and relaxed the interfaces.

Synthesis of FDT. General remarks. Commercially available chemicals were purchased and used without any further purification. Solvents were purified by standard methods and dried if necessary. 3-Bromo-5,5'-bis(trimethylsilyl)-2,2'-bithiophene **1** was prepared as previously described¹⁵. 2,7-Dibromo-9H-fluoren-9-one and bis(4-methoxyphenyl)amine were prepared following literature procedures^{55,56}. While this work was in progress, the preparation of 9-(5,5'-bis(trimethylsilyl)-2,2'-bithiophen-3-yl)-2,7-dibromo-fluoren-9-ol **2** and 2',7'-dibromospiro[cyclopenta[2,1-b:3,4-b']dithiophene-4,9'-fluorene] **3** under conditions different from those here described has been reported⁵⁷. Reactions were monitored by thin layer chromatography (TLC), which was conducted on plates precoated with silica gel Si 60-F254 (Merck). Column chromatography was conducted using silica gel Si 60, 0.063–0.200 mm (normal) or 0.040–0.063 mm (flash) (Merck, Darmstadt). ¹H and ¹³C NMR spectra were recorded on a Bruker Avance 400 (400 and 100.6 MHz, respectively); chemical shifts are indicated in parts per million downfield from SiMe₄, using the residual proton (CHCl₃ = 7.26 ppm) and carbon (CDCl₃ = 77.0 ppm) solvent resonances as the internal reference. Coupling constant values *J* are given in Hz. Proton and carbon assignments were achieved by decoupled ¹³C, ¹H–¹H double quantum filtered COSY, and ¹H–¹³C heteronuclear single quantum coherence correlation experiments. ESI mass spectra were obtained with a quadrupole time-of-flight mass spectrometer (Waters, Xevo G2-S QToF).

Synthesis of 9-(5,5'-Bis(trimethylsilyl)-2,2'-bithiophen-3-yl)-2,7-dibromo-fluoren-9-ol(2). To a solution of protected dithiophene **1** (1.54 g, 3.95 mmol) in dry Et₂O (50 ml) cooled to –78 °C, BuLi (1.6 M in hexane, 2.5 ml, 4 mmol) was added dropwise under stirring. After 2 h, a solution of 2,7-dibromo-9H-fluoren-9-one (1.11 g, 3.28 mmol) in dry THF (30 ml) was added dropwise. At the end of the addition, the cooling bath was removed and the mixture was allowed to return to room temperature and left under stirring for 4 h. After the addition of saturated aqueous NH₄Cl solution and phase separation, the organic layer was washed with water, brine, and dried over MgSO₄. After filtration, the solvent was removed at reduced pressure and the crude material was purified by flash column chromatography (silica gel, petroleum ether:CH₂Cl₂ 7:3), affording the compound **2** (1.7 g, 80% yield) as an off-white foam.

¹H NMR (400 MHz, CDCl₃): δ 7.73 (s, 1H, Thioph-H), 7.42 (*d*, *J* = 1.6 Hz, 2H, Fluor-H), 7.36 (*dd*, *J* = 8.0 Hz, *J* = 1.6 Hz, 2H, Fluor-H), 7.21 (*d*, *J* = 8.0 Hz, 2H, Fluor-H), 6.62 (*d*, *J* = 3.6 Hz, 1H, Thioph-H), 6.03 (*d*, *J* = 3.6 Hz, 1H, Thioph-H), 0.32 (s, 9H, SiCH₃), 0.29 (s, 9H, SiCH₃); ¹³C NMR (100.6 MHz, CDCl₃): δ 151.0, 142.7, 140.7, 140.6, 138.4, 137.8, 136.0, 134.4 (Thioph-C), 133.1 (Thioph-C), 132.3 (Fluor-C), 129.8 (Thioph-C), 128.5 (Fluor-C), 122.3, 121.3 (Fluor-C), 82.0, 0.1 (SiCH₃), 0.0 (SiCH₃).

Synthesis of 2',7'-Dibromospiro[cyclopenta[2,1-b:3,4-b']dithiophene-4,9'-fluorene] (3). To a suspension of FeCl₃ (70 mg, 0.43 mmol) in boiling CHCl₃ (amylene stabilized, 250 ml) carbinol **2** (560 mg, 0.86 mmol) was added. The stirred mixture became green and after 20 min the disappearance of the starting material was confirmed by TLC analysis (silica gel, petroleum ether:CH₂Cl₂ 7:3). The mixture was cooled to room temperature and the solvent, removed at reduced pressure, was recovered and reused as such for at least five subsequent runs performed on the same amount of carbinol **2**. The crude material was purified by column chromatography (silica gel, petroleum ether:CHCl₃ 9:1) to give the compound **3** (339 mg, 81% yield) as a white solid.

¹H NMR (400 MHz, CDCl₃): δ 7.63 (*d*, *J* = 8.4 Hz, 2H, Fluor-H), 7.49 (*d*, *J* = 8.4 Hz, *J* = 1.6 Hz, 2H, Fluor-H), 7.12 (*d*, *J* = 5.0 Hz, 2H, Thioph-H), 6.95 (*d*, *J* = 1.6 Hz, 2H, Fluor-H), 6.41 (*d*, *J* = 5.0 Hz, 2H, Thioph-H); ¹³C NMR (100.6 MHz, CDCl₃): δ 152.9, 147.1, 139.5, 138.9, 131.3 (Fluor-C), 126.9 (Thioph-C), 126.1 (Fluor-C), 121.8, 121.5 (Fluor-C), 121.3 (Thioph-C), 61.3.

Synthesis of 2',7'-Bis(bis(4-methoxyphenyl) amino) spiro[cyclopenta[2,1-b:3,4-b']dithiophene-4,9'-fluorene] (FDT). In a flame dried Schlenk tube the spiro derivative **3** (303.7 mg, 0.62 mmol), bis(4-methoxyphenyl)amine (315.8 mg, 1.38 mmol) and Pd₂(dba)₃ (22.2 mg, 0.024 mmol) were introduced under an inert atmosphere. The Schlenk tube was evacuated and backfilled with nitrogen three times. After the addition of toluene (5 ml) and ^tBu₃P (1M toluene solution, 25 μ l, 0.025 mmol), NaO^tBu (149 mg, 1.55 mmol) was added, and the reactor was brought into an oil bath pre-heated at 110 °C. The reaction mixture was stirred at this temperature overnight. After cooling to room temperature, the mixture was diluted with Et₂O and washed with water and brine. The organic phase was dried over MgSO₄, filtered, and the solvent removed at reduced pressure. The crude material was purified by flash column chromatography (silica gel, hexane:AcOEt 8:2) to give the compound **FDT** (400 mg, 82% yield) as an off-white solid.

¹H NMR (400 MHz, CDCl₃ + 1% v/v NH₂NH₂·H₂O): δ 7.44 (*d*, *J* = 8.4 Hz, 2H, Fluor-H), 7.05 (*d*, *J* = 5.2 Hz, 2H, Thioph-H), 6.88 (*d*, *J* = 9.2 Hz, 8H, Ar-H), 6.82 (*dd*, *J* = 8.4 Hz, *J* = 2.0 Hz, 2H, Fluor-H), 6.69 (*d*, *J* = 9.2 Hz, 8H, Ar-H), 6.51 (*d*, *J* = 5.2 Hz, 2H, Thioph-H), 6.47 (*d*, *J* = 2.0 Hz, 2H, Fluor-H), 3.74 (*s*, 12H, OCH₃); ¹³C NMR (100.6 MHz, CDCl₃ + 1% v/v NH₂NH₂·H₂O): δ 155.3, 154.9, 147.3, 146.1, 141.2, 138.2, 135.0, 125.6 (Ar-C), 125.2 (Thioph-C), 121.7 (Fluor-C), 121.3 (Thioph-C), 119.6 (Fluor-C), 116.9 (Fluor-C), 114.4 (Ar-C), 61.7, 55.5 (OCH₃). HRMS (ESI-QTOF): Calcd for (C₄₉H₃₈N₂O₄S₂)⁺ 782.2273. Found: 782.2267.

CCDC-1420477 contains the supplementary crystallographic data for this paper (see Supplementary Data). This data can be obtained free of charge from The Cambridge Crystallographic Data Centre via www.ccdc.cam.ac.uk/data_request/cif.

Received 7 September 2015; accepted 26 November 2015;
published 18 January 2016

References

- Stranks, S. D. *et al.* Electron–hole diffusion lengths exceeding 1 micrometer in an organometal trihalide perovskite absorber. *Science* **342**, 341–344 (2013).
- Ogomi, Y. *et al.* CH₃NH₃Sn_xPb_(1-x)I₃ perovskite solar cells covering up to 1060 nm. *J. Phys. Chem. Lett.* **5**, 1004–1011 (2014).
- Oga, H., Saeki, A., Ogomi, Y., Hayase, S. & Seki, S. Improved understanding of the electronic and energetic landscapes of perovskite solar cells: high local charge carrier mobility, reduced recombination, and extremely shallow traps. *J. Am. Chem. Soc.* **136**, 13818–13825 (2014).
- Xing, G. C. *et al.* Low-temperature solution-processed wavelength-tunable perovskites for lasing. *Nature Mater.* **13**, 476–480 (2014).
- Saliba, M. *et al.* Structured organic–inorganic perovskite toward a distributed feedback laser. *Adv. Mater.* <http://doi.org/f3j7p7> (2015).
- Tan, Z. K. *et al.* Bright light-emitting diodes based on organometal halide perovskite. *Nature Nanotech.* **9**, 687–692 (2014).
- Dong, R. *et al.* High-gain and low-driving-voltage photodetectors based on organolead triiodide perovskites. *Adv. Mater.* **27**, 1912–1918 (2015).
- Domanski, K. *et al.* Working principles of perovskite photodetectors: analyzing the interplay between photoconductivity and voltage-driven energy-level alignment. *Adv. Functional Mater.* **25**, 6936–6947 (2015).
- Albrecht, S. *et al.* Monolithic perovskite/silicon-heterojunction tandem solar cells processed at low temperature. *Energy Environ. Sci.* **9**, 81–88 (2016).
- Baena, J. P. C. *et al.* Highly efficient planar perovskite solar cells through band alignment engineering. *Energy Environ. Sci.* **8**, 2928–2934 (2015).
- Bailie, C. D. *et al.* Semi-transparent perovskite solar cells for tandems with silicon and CIGS. *Energy Environ. Sci.* **8**, 956–963 (2015).
- Jeon, N. J. *et al.* Compositional engineering of perovskite materials for high-performance solar cells. *Nature* **517**, 476–480 (2015).
- Saliba, M. *et al.* Influence of thermal processing protocol upon the crystallization and photovoltaic performance of organic–inorganic lead trihalide perovskites. *J. Phys. Chem. C* **118**, 17171–17177 (2014).
- Saliba, M. *et al.* Plasmonic-induced photon recycling in metal halide perovskite solar cells. *Adv. Funct. Mater.* **25**, 5038–5046 (2015).
- Horantner, M. T., Zhang, W., Saliba, M., Wojciechowski, K. & Snaith, H. J. Templated microstructural growth of perovskite thin films via colloidal monolayer lithography. *Energy Environ. Sci.* **8**, 2041–2047 (2015).
- Burschka, J. *et al.* Sequential deposition as a route to high-performance perovskite-sensitized solar cells. *Nature* **499**, 316–319 (2013).
- Malinkiewicz, O. *et al.* Perovskite solar cells employing organic charge-transport layers. *Nature Photon.* **8**, 128–132 (2014).
- Yang, W. S. *et al.* High-performance photovoltaic perovskite layers fabricated through intramolecular exchange. *Science* **348**, 1234–1237 (2015).
- Ahn, N. *et al.* Highly reproducible perovskite solar cells with average efficiency of 18.3% and best efficiency of 19.7% fabricated via Lewis base adduct of lead(II) iodide. *J. Am. Chem. Soc.* **137**, 8696–8699 (2015).
- Bach, U. *et al.* Solid-state dye-sensitized mesoporous TiO₂ solar cells with high photon-to-electron conversion efficiencies. *Nature* **395**, 583–585 (1998).
- Murray, A. T. *et al.* Modular design of SPIRO-OMeTAD analogues as hole transport materials in solar cells. *Chem. Commun.* **51**, 8935–8938 (2015).
- Abate, A. *et al.* Silolothiophene-linked triphenylamines as stable hole transporting materials for high efficiency perovskite solar cells. *Energy Environ. Sci.* **8**, 2946–2953 (2015).
- Ganesan, P. *et al.* A simple spiro-type hole transporting material for efficient perovskite solar cells. *Energy Environ. Sci.* **8**, 1986–1991 (2015).
- Jeon, N. J. *et al.* *o*-Methoxy substituents in Spiro-OMeTAD for efficient inorganic–organic hybrid perovskite solar cells. *J. Am. Chem. Soc.* **136**, 7837–7840 (2014).
- Liu, J. *et al.* A dopant-free hole-transporting material for efficient and stable perovskite solar cells. *Energy Environ. Sci.* **7**, 2963–2967 (2014).
- Zheng, L. L. *et al.* A hydrophobic hole transporting oligothiophene for planar perovskite solar cells with improved stability. *Chem. Commun.* **50**, 11196–11199 (2014).
- Petrus, M. L., Bein, T., Dingemans, T. J. & Docampo, P. A low cost azomethine-based hole transporting material for perovskite photovoltaics. *J. Mater. Chem. A* **3**, 12159–12162 (2015).
- Ito, S., Tanaka, S. & Nishino, H. Lead-halide perovskite solar cells by CH₃NH₃I dripping on PbI₂–CH₃NH₃I–DMSO precursor layer for planar and porous structures using CuSCN hole-transporting material. *J. Phys. Chem. Lett.* **6**, 881–886 (2015).
- Zhao, D. W. *et al.* High-efficiency solution-processed planar perovskite solar cells with a polymer hole transport layer. *Adv. Energy Mater.* **5**, 1401855 (2015).
- Krishna, A. *et al.* Novel hole transporting materials based on triptycene core for high efficiency mesoscopic perovskite solar cells. *Chem. Sci.* **5**, 2702–2709 (2014).
- Krishna, A. *et al.* Facile synthesis of a furan-arylamine hole-transporting material for high-efficiency, mesoscopic perovskite solar cells. *Chemistry* **21**, 15113–15117 (2015).
- Li, H. R. *et al.* A simple 3,4-ethylenedioxythiophene based hole-transporting material for perovskite solar cells. *Angew. Chem. Int. Ed.* **53**, 4085–4088 (2014).
- Lim, I. *et al.* Indolocarbazole based small molecules: an efficient hole transporting material for perovskite solar cells. *RSC Adv.* **5**, 55321–55327 (2015).
- Ball, J. M. *et al.* Optical properties and limiting photocurrent of thin-film perovskite solar cells. *Energy Environ. Sci.* **8**, 602–609 (2015).
- Pozzi, G. *et al.* Synthesis and Photovoltaic Applications of a 4,4'-Spiro[bicyclopenta[2,1-b;3,4-b']dithiophene]-bridged donor/acceptor dye. *Org. Lett.* **15**, 4642–4645 (2013).
- Malinauskas, T. *et al.* Enhancing thermal stability and lifetime of solid-state dye-sensitized solar cells via molecular engineering of the hole-transporting material Spiro-OMeTAD. *ACS Appl. Mater. Inter.* **7**, 11107–11116 (2015).
- Torres, A. & Rego, L. G. C. Surface effects and adsorption of methoxy anchors on hybrid lead iodide perovskites: insights for Spiro-MeOTAD attachment. *J. Phys. Chem. C* **118**, 26947–26954 (2014).
- Yin, J. *et al.* Interfacial charge transfer anisotropy in polycrystalline lead iodide perovskite films. *J. Phys. Chem. Lett.* **6**, 1396–1402 (2015).
- Pastore, M., Mosconi, E. & De Angelis, F. Computational investigation of dye-iodine interactions in organic dye-sensitized solar cells. *J. Phys. Chem. C* **116**, 5965–5973 (2012).
- Umari, P., Mosconi, E. & De Angelis, F. Relativistic GW calculations on CH₃NH₃PbI₃ and CH₃NH₃SnI₃ perovskites for solar cell applications. *Sci. Rep.* **4**, 4467 (2014).
- Abate, A. *et al.* Lithium salts as “redox active” p-type dopants for organic semiconductors and their impact in solid-state dye-sensitized solar cells. *Phys. Chem. Phys.* **15**, 2572–2579 (2013).
- Unger, E. L. *et al.* Hysteresis and transient behavior in current–voltage measurements of hybrid-perovskite absorber solar cells. *Energy Environ. Sci.* **7**, 3690–3698 (2014).
- Christians, J. A., Manser, J. S. & Kamat, P. V. Best practices in perovskite solar cell efficiency measurements. Avoiding the error of making bad cells look good. *J. Phys. Chem. Lett.* **6**, 852–857 (2015).
- Sheng, R. *et al.* Methylammonium lead bromide perovskite-based solar cells by vapor-assisted deposition. *J. Phys. Chem. C* **119**, 3545–3549 (2015).
- Chueh, C. C. *et al.* Non-halogenated solvents for environmentally friendly processing of high-performance bulk-heterojunction polymer solar cells. *Energy Environ. Sci.* **6**, 3241–3248 (2013).
- Osedach, T. P., Andrew, T. L. & Bulovic, V. Effect of synthetic accessibility on the commercial viability of organic photovoltaics. *Energy Environ. Sci.* **6**, 711–718 (2013).
- Becke, A. D. Density—functional thermochemistry. III. The role of exact exchange. *J. Chem. Phys.* **98**, 5648–5652 (1993).
- Petersson, G. A. & Al-Laham, M. A. A complete basis set model chemistry. II. Open-shell systems and the total energies of the first-row atoms. *J. Chem. Phys.* **94**, 6081–6090 (1991).
- Perdew, J. P., Burke, K. & Ernzerhof, M. Generalized gradient approximation made simple. *Phys. Rev. Lett.* **77**, 3865–3868 (1996).
- Soler, J. M. *et al.* The SIESTA method for *ab initio* order-*N* materials simulation. *J. Phys. Condens. Matter* **14**, 2745–2779 (2002).
- Wu, Z. G. & Cohen, R. E. More accurate generalized gradient approximation for solids. *Phys. Rev. B* **73**, 235116 (2006).
- Collella, S. *et al.* Elusive presence of chloride in mixed halide perovskite solar cells. *J. Phys. Chem. Lett.* **5**, 3532–3538 (2014).
- Mosconi, E., Ronca, E. & De Angelis, F. First-principles investigation of the TiO₂/organohalide perovskites interface: the role of interfacial chlorine. *J. Phys. Chem. Lett.* **5**, 2619–2625 (2014).

54. Mitzi, D. B. Solution-processed inorganic semiconductors. *J. Mater. Chem.* **14**, 2355–2365 (2004).
55. Marzari, G. *et al.* Fluorous molecules for dye-sensitized solar cells: synthesis and characterization of fluorene-bridged donor/acceptor dyes with bulky perfluoroalkoxy substituents. *J. Phys. Chem. C* **116**, 21190–21200 (2012).
56. Zhang, X., Han, J. B., Li, P. F., Ji, X. & Zhang, Z. Improved, highly efficient, and green synthesis of bromofluorenes and nitrofluorenes in water. *Synth. Commun.* **39**, 3804–3815 (2009).
57. Jeux, V., Dalinot, C., Allain, M., Sanguinet, L. & Leriche, P. Synthesis of Spiro[cyclopenta[1,2-b:5,4-b']DiThiophene-4,9'-Fluorenes] SDTF dissymmetrically functionalized. *Tetrahedron Lett.* **56**, 1383–1387 (2015).

Acknowledgements

This work was supported by the European Union Seventh Framework Programme [FP7/2007–2013] under grant agreement no 604032 of the MESO project, (FP7/2007–2013) ENERGY.2012.10.2.1; NANOMATCELL, grant agreement no. 308997. M.K.N. acknowledges funding by the Swiss National Science Foundation under NRP 70, grant No: 407040_154056, and MG Nanotera. We thank A. Wakamiya, Institute for Chemical Research, Kyoto University Uji, Kyoto 611-0011, Japan, F. Giordano for

experimental help with lithium doping of the TiO₂ scaffold, and T. Schmaltz for helpful discussions.

Author contributions

M.S. and T.M. conceived and designed the experiments, including fabrication and measurement of the PV devices. M.S. conducted DSC and TGA measurements. S.O., M.C. and G.P. designed and synthesized the FDT hole-transporting material. S.A. and P.G. developed crystals and characterized the FDT. J.-P.C.-B. and A.A. optimized TiO₂ photoanodes, the perovskite films and characterized SEM. E.M. and F.D.A. performed first-principles calculations. R.S. analysed single crystals. M.S. wrote the first draft of the paper. All the authors contributed to the discussion and the writing of the paper, and approved. M.K.N. directed the scientific research for this work.

Additional information

Supplementary information is available [online](http://www.nature.com/online). Reprints and permissions information is available online at www.nature.com/reprints. Correspondence and requests for materials should be addressed to M.K.N.

Competing interests

The authors declare no competing financial interests.